Ferroelectricity in Epitaxial Tetragonal ZrO2 Thin Films

Ali El Boutaybi, Thomas Maroutian, Ludovic Largeau, Nathaniel Findling, Jean-blaise Brubach, Rebecca Cervasio, Alban Degezelle, Sylvia Matzen, Laurent Vivien, Pascale Roy, et al.

ADVANCED ELECTRONIC MATERIALS Open Access
www.advelectronicmat.de

Ferroelectricity in Epitaxial Tetragonal ZrO_2 Thin Films

Ali El Boutaybi, Thomas Maroutian, Ludovic Largeau, Nathaniel Findling, Jean-Blaise Brubach, Rebecca Cervasio, Alban Degezelle, Sylvia Matzen, Laurent Vivien, Pascale Roy, Panagiotis Karamanis, Michel Rérat, and Philippe Lecoeur*

The crystal structure and ferroelectric properties of epitaxial ZrO_2 films ranging from 7 to 42 nm thickness grown on $La_{0.67}Sr_{0.33}MnO_3$ buffered (110)-oriented $SrTiO_3$ substrate are reported. By employing X-ray diffraction, a tetragonal phase (t-phase) at all investigated thicknesses, with slight in-plane strain due to the substrate in the thinnest films, is confirmed. Further confirmation of the t-phase is obtained through infrared absorption spectroscopy with synchrotron light, performed on ZrO_2 membrane transferred onto a high resistive silicon substrate. Up to a thickness of 31 nm, the ZrO_2 epitaxial films exhibit ferroelectric behavior, at variance with the antiferroelectric behavior reported previously for the t-phase in polycrystalline films. However, the ferroelectricity is found here to diminish with increasing film thickness, with a polarization of 13 μC cm^{-2} and down to 1 μC cm^{-2} for 7 and 31 nm thick ZrO_2 films, respectively. Given that the t-phase is nonpolar, the observations emphasize the influence of external factors, in promoting polarization in t-ZrO_2 thin films. These findings provide new insights into the ferroelectric properties and structure of ZrO_2 thin films, and open up new directions to investigate the origin of ferroelectricity in ZrO_2 and to optimize this material for future applications.

1. Introduction

The discovery of ferroelectricity in Si-doped HfO_2 has expanded the research on HfO_2 and ZrO_2 beyond their conventional role as high-k dielectric materials.[1] These materials have been extensively investigated for various microelectronic applications[] and are thermodynamically stable when in contact with silicon,[3] making them compatible with metal-oxide-semiconductor (CMOS) technology.[4,5] Thanks to their ferroelectric behavior HfO_2 and ZrO_2-based compounds have demonstrated potential in various technological fields, offering opportunities for advancements in electronic devices.[5–13] Antiferroelectricity has also been reported in ZrO_2 and ZrO_2-rich compounds, which further expands the prospects for these materials.[14,15]

Commonly reported polar phases of HfO_2 and ZrO_2 are the orthorhombic $Pbc2_1$ (*o*-phase) and rhombohedral $R3m$ (*r*-phase) phases.[1,16] However, these polar phases are metastable, and several approaches have been employed to stabilize these ferroelectric phases. One commonly used approach is through doping and controlling the grain size.[17,18] Doping alone may not necessarily stabilize the polar phase,[19,20] but it can alter its surface energy, which in turn may affect its stability and sometimes enhance the polarization. Therefore, even with doping, the grain size still plays a role in stabilizing the ferroelectric state in these materials, with surface effects playing a crucial role.[21–23]

In recent years, the ferroelectric properties of pure ZrO_2 have garnered considerable attention, primarily due to its resemblance to HfO_2, as well as its greater abundance in nature compared to HfO_2.[24] Notably, investigations of ZrO_2 have been conducted in various forms, such as pure ZrO_2 in polycrystalline thin films, leading to the identification of the *o*-phase.[25–28] The same *o*-phase has also been observed in epitaxial thin films,[29] for which both the *r*-phase[23,30] and the $P4_2/nmc$ t-phase (*t*-phase)[31] have been reported as well. Indeed, when the grain size is reduced to the nanoscale (<30 nm), the stable phase of ZrO_2 is the nonpolar *t*-phase.[32–34] This is attributed to the lower surface enthalpy of *t*-ZrO_2 compared to the ground state monoclinic $P2_1/c$ phase (*m*-phase) of ZrO_2.[34] However, in thinner ZrO_2 films, polar phases (*o* and *r*) have been reported, as mentioned above. Thus, the stabilization of polar phases in these nanocrystalline materials involves a competition between various polymorphs, including both polar and nonpolar phases. It is worth noting that

A. El Boutaybi, T. Maroutian, L. Largeau, N. Findling, A. Degezelle, S. Matzen, L. Vivien, P. Lecoeur
Centre de Nanosciences et de Nanotechnologies (C2N)
Universite Paris-Saclay, CNRS
Palaiseau 91120, France
E-mail: ali.el-boutaybi@c2n.upsaclay.fr
J.-B. Brubach, R. Cervasio, P. Roy
Synchrotron SOLEIL - CNRS - CEA Paris-Saclay
Palaiseau 91120, France
P. Karamanis, M. Rérat
Université de Pau et des Pays de l'Adour, CNRS, IPREM, E2S UPPA
Pau 64012, France
The ORCID identification number(s) for the author(s) of this article can be found under https://doi.org/10.1002/aelm.202300516

DOI: 10.1002/aelm.202300516

increasing the thickness without maintaining and controlling a proper grain size can lead to degradation and suppression of the ferroelectric behavior.[35,36]

In addition to the ferroelectric state, antiferroelectricity has also raised significant interest recently, particularly in ZrO_2-rich thin films. However, the origin of antiferroelectric phases is less studied compared to ferroelectric ones. First, orthorhombic *Pbca* could potentially contribute to the observed antiferroelectric behavior in ZrO_2,[37] as this phase is a combination of two unit cells of the polar *o*-phase with opposite polarizations.[22,38,39] This phase is also found to be energetically close to the ground state *m*-phase.[39,40] Additionally, the *t*-phase has been identified as a potential driver of antiferroelectric behavior in ZrO_2 polycrystalline thin films[41]; this has been explained as a transition from the nonpolar *t*-phase to the polar *o*-phase.[41] This second approach is the most commonly adopted in the literature.[15,27,42–44]

In this study, we demonstrate the ferroelectricity of *t*-phase ZrO_2 thin films with varying thicknesses ranging from 7 to 42 nm. First, the *t*-phase of ZrO_2 is evidenced by X-ray Diffraction (XRD). Then, synchrotron Infrared (IR) absorbance spectroscopy confirms the same *t*-phase. To better understand the IR bands in our experimental results, we used first-principles calculations with the CRYSTAL suite of programs to investigate the IR activities and simulate the IR absorbance of *t*-ZrO_2.[45] The details about the calculations can be found in Ref. [46]. Finally, we show that ZrO_2 thin films exhibit ferroelectric behavior up to a thickness of 31 nm, indicating the development of polarization in a nonpolar *t*-phase when the film thickness is reduced. In line with studies on *r*- and *o*-phase epitaxial thin films,[16,23,29,30] the ferroelectric behavior is here obtained in the pristine *t*-phase films, directly after growth, and thus do not correspond to a change to another crystalline phase upon field cycling.[31]

2. Experimental Section

2.1. Sample Fabrication

Thin films of pure ZrO_2 ranging from 7 to 42 nm thickness were grown on (110)-oriented $SrTiO_3$ (STO) substrate with a $La_{0.67}Sr_{0.33}MnO_3$ (LSMO) buffer layer using pulsed laser deposition (PLD). The deposition was performed at a temperature of 800 °C, under an O_2 growth pressure of 0.1 mbar for ZrO_2 and 0.18 mbar for LSMO films, and with a laser energy fluence of 1.1 J cm^{-2} at a repetition rate of 2 Hz. The target–substrate distance was maintained at 6 cm. The as-grown films were cooled down to room temperature at a rate of 10 °C min^{-1}.

Due to the large IR response of STO,[47] the IR measurements were performed on a ZrO_2 membrane, which was obtained by chemically etching the LSMO bottom electrode to release the ZrO_2 film from the STO substrate. Subsequently, the ZrO_2 film was transferred onto a high-resistivity silicon substrate (Si-HR) for IR measurement.

2.2. Structure Analysis

The crystal structure and epitaxial orientation of the thin films were analyzed using XRD techniques. For $\theta - 2\theta$ out-of-plane scans, a Panalytical X'pert Pro diffractometer was utilized

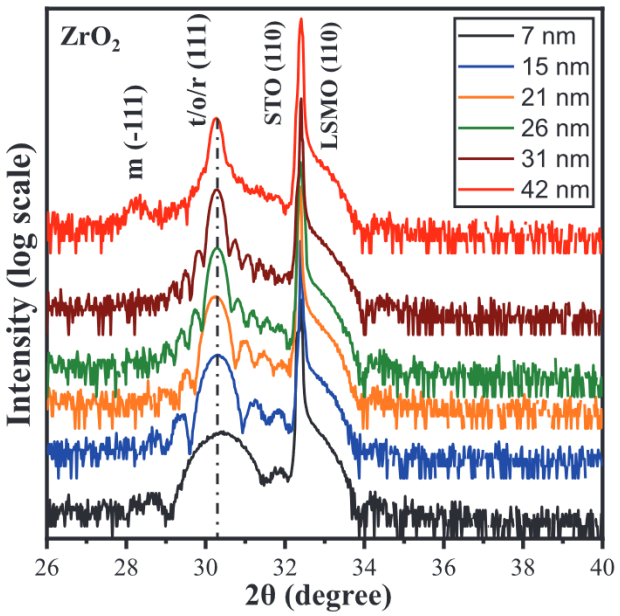

Figure 1. Out-of-plane X-Ray diffraction, $\theta - 2\theta$ of pure ZrO_2 at different thicknesses.

(**Figure 1**), while other XRD analyses were performed in a non-coplanar geometry using a Rigaku SmartLab diffractometer. Both diffractometers were configured in a parallel beam setup and employed monochromated Cu $K\alpha_1$ radiation with a wavelength of 1.54059 Å.

In addition, IR spectroscopy was employed to investigate the phonon activities of the ZrO_2 membrane, specifically the IR absorbance of ZrO_2 in transmission configuration. The IR measurements were performed at the AILES beamline of synchrotron SOLEIL with a Bruker IFS125 FT-IR spectrometer. Spectra in the far infrared region (20–700 cm^{-1}) were obtained by using a 6 µm-thick Mylar beam splitter and a 4.2*K* bolometer detector. Absorbance spectra were recorded with a resolution of 2 cm^{-1}, at 4 cm s^{-1} mirror speed, and by averaging 200 scans.[48]

2.3. Ferroelectric Characterization

To measure the ferroelectric properties of the films, platinum/ZrO_2(film)/ LSMO capacitors were fabricated using standard photolithography and lift-off techniques. The capacitors were then characterized using a ferroelectric tester (AixACCT, TF analyzer 1000). The film's ferroelectric response was obtained through Positive Up Negative Down (PUND) measurements. The polarization–electric field (P-E) loops were measured at a frequency of 1 kHz with a triangular waveform.

3. Results and Discussion

3.1. ZrO_2 Thin Films

Figure 1 shows the $\theta - 2\theta$ out-of-plane XRD of ZrO_2 thin films at different thicknesses ranging from 7 to 42 nm. The most intense peaks correspond to the (110)-oriented STO substrate, while the

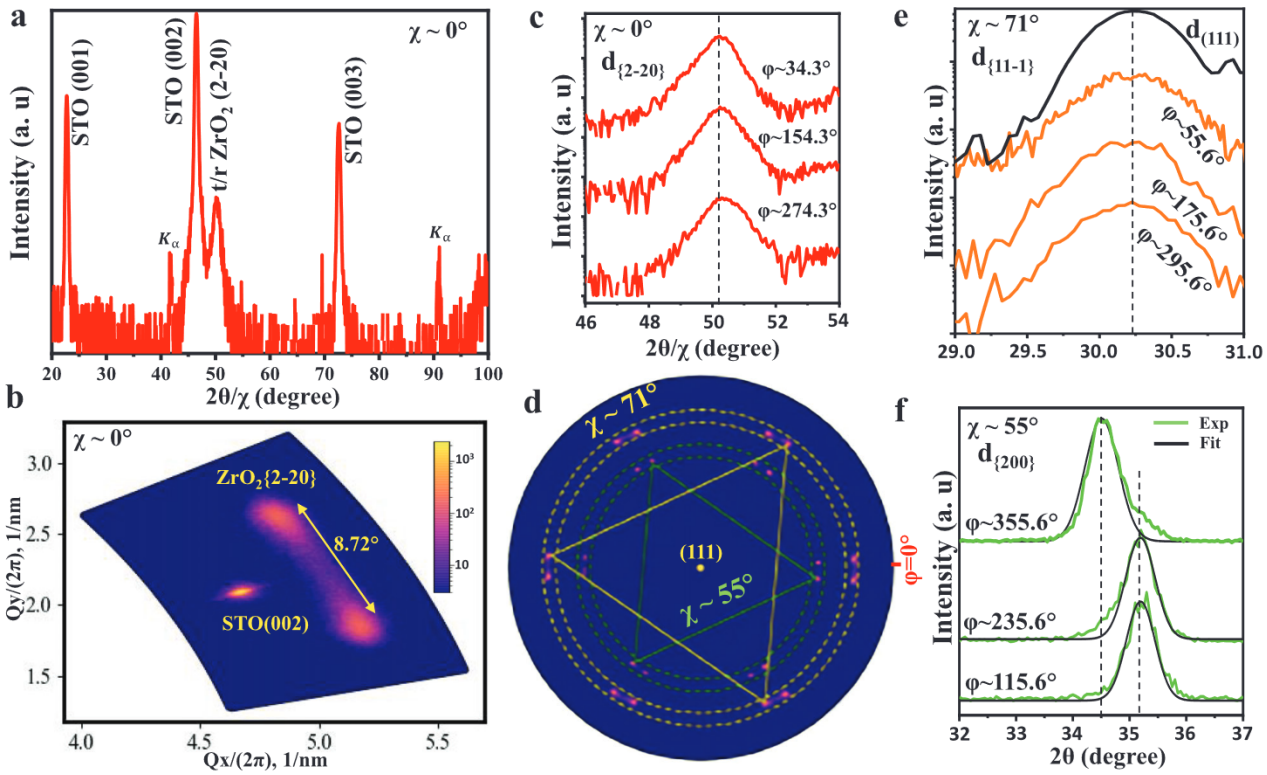

Figure 2. X-ray diffraction measurements performed on a 15 nm thick pure ZrO_2 thin film: a) in-plane $\theta - 2\theta$ scan along the <001>STO azimuthal direction, b) reciprocal space map ($2\theta - \phi$ scan) around the (002) STO plane, c) in-plane $\theta - 2\theta$ scan for one variant observed in (b), d) pole figures measured at $2\theta = 30.30°$ and 34.5°, e) $\theta - 2\theta$ scan for one variant observed at around $\chi = 71°$ (highlighted in yellow in pole figure), and f) $\theta - 2\theta$ scan for one variant observed at $\chi = 55°$ (highlighted in green in pole figure).

peaks closest to the substrate correspond to the (110) pseudo-cubic orientation of the LSMO bottom electrode. The thickness of LSMO was determined to be close to 20 nm using X-ray reflectivity. At a 2θ angle of about 30.30°, the (111) peak of ZrO_2 is observed, which can correspond to the *o*-, *r*-, or *t*-phases. It should be noted that this peak around 30° is ascribed to the *o*-phase or *r*-phase when the films exhibit ferroelectric behavior.[1,16,23,29,30] In Figure 1, it can be observed that for a ZrO_2 film of 42 nm thickness, the ground state *m*-phase is observed at $2\theta = 28.32°$; similar thickness dependence has been reported for ZrO_2 *r*-phase.[23] In all ZrO_2 thin films, the (111) peak is observed at the same 2θ of 30.30°. Only in the thinnest film of 7 nm, this peak appears slightly shifted to the right, indicating a small tensile strain in the film, as expected for the (110)-STO substrate.[49] Note that, for easy comparison between ZrO_2 phases, here for the *t*-phase we adopted a pseudo-cubic representation described by 12 atoms in a unit cell; however, the *t*-phase can also be described using six atoms, and in this case the peak at 30.30° will correspond to the (101) plane.

Further XRD measurements were conducted to gain insight into the phase and symmetry of ZrO_2 thin films. In particular, to distinguish between the different possible phases of ZrO_2, specific families of crystallographic planes can be analyzed. For instance, the {1 − 10} planes are not present in the *t*-phase, whereas they are present in the *m*-, *o*-, and *r*-phases. In the *r*-phase, these planes are all present but with low intensity due to the high symmetry of the phase, and, accordingly, these planes were not reported in ZrO_2 *r*-phase.[23] However, the *r*-phase has equal lattice parameters, a = b = c, which make it distinguishable from other phases. The same is true for the *m*-phase, which can be easily identified from XRD analysis (Figure 1 in red). On the other hand, the *o*-phase has a lattice parameter close to the one of the *t*-phase, making it challenging to distinguish it from the *t*-phase based only on the unit cell lattice parameters. Thus, the main difference by XRD between the *t*- and *o*- phases is the presence of the {1 − 10} family planes in the *o*-phase.[50]

First, to obtain the film orientation with respect to the substrate and detect any other phases, in-plane XRD measurements were conducted along the <001 > of STO azimuthal direction. These measurements are known to be more sensitive to sample size than film thickness, allowing to detect other phases that may be present at the film/substrate interface or in small amounts in the thin film, as previously observed in ZrO_2 and $Hf_{0.5}Zr_{0.5}O_2$ (HZO) on (001)-oriented STO substrate.[23] **Figure 2**a displays the in-plane XRD of 15 nm-thick ZrO_2 along <001 > azimuthal direction, where an additional peak at a 2θ of 50.15° is observed. This peak can correspond to the *r*- or *t*-phase. For the *o*-phase, a peak at 24.5° is expected for the (1-10) plane,[50] although only one plane from the {1 − 10} family of $Pbc2_1$ phase is allowed by symmetry reasons.

It is worth noting that the alignment of ZrO_2 films with the substrate does not follow a specific direction of the latter. Indeed, the peak observed at 50.15° is not precisely aligned with the (001) direction of the STO substrate. An in-plane 2D ($2\theta - \phi$)

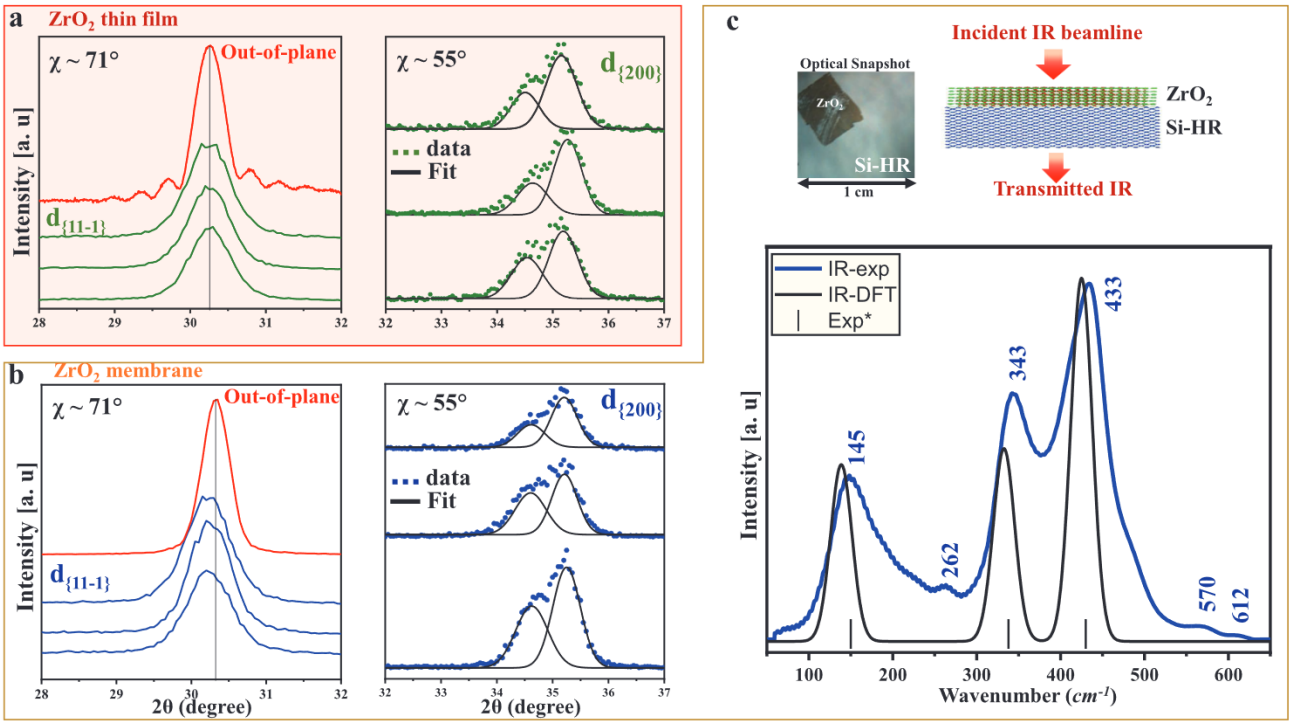

Figure 3. X-Ray diffraction and IR measurements performed on a 26 nm-thick pure ZrO_2: a) $\theta - 2\theta$ Bragg scans performed on ZrO_2 thin film for {111} and {200} crystal planes at $\chi = 71°$ and $\chi = 55°$, respectively. b) Same Bragg scans obtained on ZrO_2 membrane for the {111} and {200} crystal planes at $\chi = 71°$ and $\chi = 55°$, respectively. c) Experimental IR absorbance of ZrO_2 membrane, with the peak positions (in cm^{-1}) indicated in blue. The IR absorbance obtained using the CRYSTAL code is also provided for the *t*-phase. *Additionally, earlier experimental IR results for the *t*-phase taken from Ref. [55] are indicated.

map was performed around the (002)-STO plane, as presented in Figure 2b, demonstrating that the (2-20) plane is rotated by 4.3° relative to the (001)-STO direction. This finding is also supported by the pole figures generated at $2\theta = 34.5°$ and $2\theta = 30.30°$ (Figure 2d). The appearance of two spots in Figure 2b indicates the existence of another {2 − 20} plane family, which is rotated by 8.72° relative to the first spot. This epitaxial relationship has also been reported in HZO films on (110)-STO substrates with a similar angle of rotation (8.5°),[51] and is further discussed in Ref. [52]. The split into different variants observed at a given angle (Figure 2b) may represent a way for the ZrO_2 film to minimize its energy. Additionally, it is important to mention that ZrO_2 thin films (and HfO_2 as well) do not exhibit direct epitaxy on perovskite substrates but rather follow a domain-matching epitaxy.[53] Further, the in-plane ϕ scan around {2 − 20} planes results in 12 peaks (see Figure S1, Supporting Information). Taking one variant and performing Bragg scans (Figure 2c) reveals the close interatomic distance between these planes ($d_{(20-2)} \approx d_{(0-22)} \approx 1.885$ Å and $d_{(2-20)} \approx 1.871$ Å), suggesting that the phase of ZrO_2 is tetragonal.

The absence of the {1 − 10} family planes in Figure 2a indicates that the peak at $2\theta \approx 50.15°$ corresponds to the *t*-phase, although the possibility of the *r*-phase cannot be entirely ruled out, given its low structure factor intensity for {1 − 10} planes (see Table S1, Supporting Information). To verify that the absence of {1 − 10} planes is not solely due to in-plane measurements taken in a specific azimuthal direction (<001 > of STO), an identical in-plane 2D ($2\theta - \phi$) map, as the one shown in Figure 2b, was performed around the (001)-STO, and the {1 − 10} plane is expected to diffract at 24.5° if present. The result is provided in Figure S1 (Supporting Information), confirming the absence of the {1 − 10} plane. Furthermore, to ensure that the {1 − 10} plane is absent throughout the entire film, a pole figure was conducted around a 2θ angle of 24.5° (Figure S1, Supporting Information), which also confirms the lack of signal for the {1 − 10} plane. Notably, the (1 − 10) of the *m*-phase was easily observed in thick ZrO_2 (42 nm) and 10 nm-thick pure HfO_2 (see Supporting Information), exhibiting a structure factor intensity close to that of the *o*-phase (see Table S1, Supporting Information). Finally, it should be noted that the (1 − 10) plane of the *o*-phase was readily identified in 10 nm-thick Y-doped HfO_2.[50] Therefore, the absence of detection of the (1-10) plane in the 15 nm-thick ZrO_2 film supports the conclusion that its phase does not belong to the orthorhombic system.

At this stage, the close relationship between the *t*- and *r*-phases, particularly when the film is (111) oriented, underscores the necessity for additional structural analysis to comprehend the crystal structure of ZrO_2. Even though in the *r*-phase, the $d_{(2-20)}$, $d_{(20-2)}$, and $d_{(02-2)}$ should be similar, the twofold symmetry of (110)-oriented STO substrate can induce such difference as observed in Figure 2c. For this, one can investigate the {11 − 1} planes, which provide information about the angle of the unit cell.[16] In the *r*-phase, the difference in interatomic distance between $d_{(111)}$ and $d_{\{11-1\}}$ gives a unit cell angle below 90°.[16,23] In contrast, in the *t*- and also in the *o*-phase, $d_{(111)}$ and $d_{\{11-1\}}$ are equal, yielding a unit cell angle of 90°.

Table 1. Lattice parameters a, b, and c of 15, 26, and 42 nm-thick ZrO_2 thin films.

	a [Å]	b [Å]	c [Å]	Tetragonality (c/a)
ZrO_2 (15 nm)	5.096	5.096	5.195	1.019
ZrO_2 (26 nm)	5.088	5.089	5.183	1.019
ZrO_2 (26 nm)[a)]	5.089	5.089	5.184	1.019
ZrO_2 (42 nm)	5.085	5.085	5.187	1.020
ZrO_2[54]	5.074	5.074	5.188	1.022

[a)] Lattice parameters of 26 nm thick ZrO_2 membrane.

To investigate the {11 − 1} planes, a pole figure was generated at $2\theta = 30.30°$, and the result is shown in Figure 2d (12 spots are found at $\chi \approx 71°$). The pole figure confirms the angle between the two twins (8.7°), as observed in the in-plane 2D maps (Figure 2b), and reveals the presence of four ZrO_2 variants in the film. Focusing on one variant, the Bragg scans ($\theta - 2\theta$ scans) of the {11 − 1} planes are provided in Figure 2e. The interatomic distances of the {111} (out-of-plane) and the {11 − 1} (at $\chi \approx 71°$) planes are almost the same, with only a small tensile distortion, giving a unit cell angle of 90.07° (0.05). This small distortion of the unit cell can be induced by tensile strain caused by the substrate. This measurement indicates that the phase is not rhombohedral.

Based on previous investigations, the ZrO_2 film on (110)-STO is tetragonal. To determine the lattice parameters of this tetragonal unit cell, a pole figure was performed at $2\theta = 34.5°$, and is given in Figure 2d (highlighted in green). One variant was selected to examine the *a*, *b*, and *c* parameters, while the other variants are given in the Supporting Information. Figure 2f displays the $\theta - 2\theta$ scans for one variant, showing two similar peaks corresponding to *a* and *b* lattice parameters, and a peak at a clearly different 2θ value corresponding to the *c* parameter of the *t*-phase. The extracted lattice parameters are $a \sim b = 5.096$Å and $c = 5.195$Å, which fall close to the values reported for *t*-ZrO_2 in the literature.[54]

Furthermore, Figure 2f shows that the peak at $\phi = 235.6°$ appears to extend on the lower 2θ side, while the peak at $\phi = 355.6°$ has a shoulder on the higher 2θ side, suggesting the possibility of mixed lattice parameters in one crystallographic direction. In the 42 nm-thick ZrO_2 film (see Supporting Information), double peaks were indeed observed along each of the 3 azimuths, indicating the presence of two lattice parameters. This finding suggests the existence of not only four but 12 variants in 42 nm thick ZrO_2. This was also observed in 26 nm thick ZrO_2 film, as will be discussed below (**Figure 3**). This increase in variant number with increasing film thickness suggests that this is a way for the ZrO_2 thin films to relax the strain. It is important to note that similar double peaks were also observed in a 10 nm thick Y-doped HfO_2 thin film.[50] Here, in the case of pure ZrO_2, they are hardly observed in a 15 nm thick film (Figure 2f) and clearly observed in thicker (>15nm) ones (see Figure 3 and Supporting Information).

Table 1 displays the extracted lattice parameters of ZrO_2 at different thicknesses. The lattice parameters are slightly higher at a thickness of 15 nm than at 42 nm, indicating a small tensile strain in thinner films. As the thickness increases to 42 nm, the lattice parameters approach those reported for ZrO_2 in powder form, as reported in Ref. [54] (also listed in Table 1).

3.2. ZrO_2 Membrane

In addition to XRD measurements, IR spectroscopy offers an alternative method for characterizing the crystal structure of materials by examining their phonon activities, which act as distinctive fingerprints for each crystal symmetry. Notably, IR spectroscopy has demonstrated its capability to identify and differentiate between different ZrO_2 phases.[46,56] To perform IR characterization, a 26 nm thick ZrO_2 film was transferred onto a Si-HR substrate (as shown in the snapshot insert in Figure 3c). The use of Si-HR, which is transparent in the IR region, allows access to the absorbance response of ZrO_2, facilitating precise analysis of its properties. The same measurement was performed first for the ZrO_2/LSMO/STO stack; however, no signal could be obtained, primarily because STO is not transparent in the IR region and also due to its considerable thickness.

Before conducting IR absorbance measurements on ZrO_2/Si-HR, XRD analyses were performed both before and after the transfer of the ZrO_2 film to investigate the impact of the release on the film structure. Figure 3a,b depicts $\theta - 2\theta$ Bragg scans carried out on the ZrO_2 thin film and ZrO_2 membrane, focusing on the {11 − 1} and {200} crystal planes at $\chi = 71°$ and $\chi = 55°$, respectively. As previously mentioned, the {200} $\theta - 2\theta$ Bragg scans reveal the presence of double peaks in thick ZrO_2, indicating a combination of two lattice parameters in one given crystallographic direction. The extracted lattice parameters are displayed in Table 1, confirming a t-phase in both ZrO_2 film and membrane. However, a noteworthy distinction emerges when examining the $\theta - 2\theta$ Bragg scans around {111}, indicating no distortion in the ZrO_2 thin film with unit cell angle ≈90° (0.05°), while in the ZrO_2 membrane, a distorted unit cell angle ≈90.20° (0.05°) is obtained, corresponding to tensile strain. Conversely, the lattice parameters *a*, *b*, and *c* exhibit minimal changes upon releasing the ZrO_2 film to obtain the membrane, as illustrated in Table 1.

The utilization of XRD enabled us to confirm that releasing a ZrO_2 film from its substrate does not alter its crystal structure, but does induce some additional strain, as evidenced in Figure 3a,b. Subsequently, the *t*-phase of ZrO_2 was further substantiated through IR absorbance spectroscopy. As presented in Figure 3c, it revealed the presence of the three main characteristic bands of the *t*-phase of ZrO_2,[22,46] in excellent agreement with earlier experimental findings reported in Ref. [55] (also depicted in bar form in Figure 3c). The IR absorbance of the ZrO_2 *t*-phase is also confirmed by our theoretical IR absorbance calculated using the CRYSTAL17 package, as given in black in Figure 3c. Specifically, the experimentally observed values of the three main IR bands, as indicated in Figure 3c, are in good agreement with the theoretical ones at 139, 333, and 426 cm^{-1}, for E_u , $A2u$, and E_u IR phonon modes of the ZrO_2 *t*-phase, respectively. The simulated theoretical intensities also closely match the experimental ones (Figure 3c). Furthermore, the two lower IR bands with low intensity also agree well with previous calculations, as reported in Refs. [22, 46].

In addition to the clear observation of the three characteristic IR absorbance bands of the *t*-phase, three additional bands

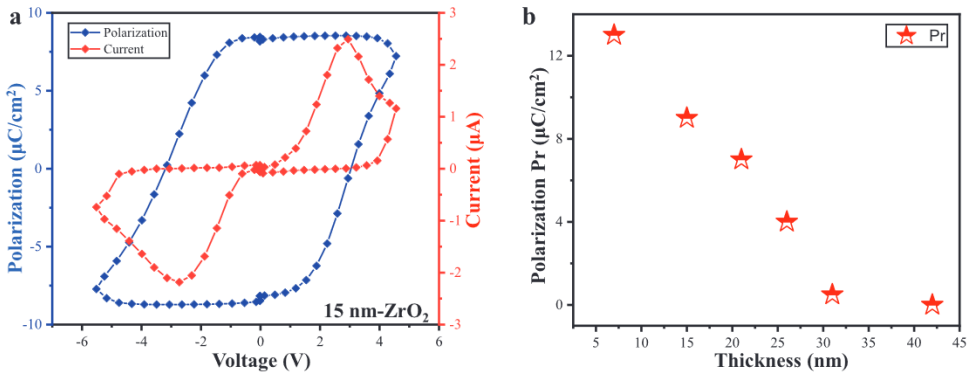

Figure 4. a) Polarization hysteresis loop of 15 nm thick pure ZrO_2 thin film, and b) remanent polarization Pr value at different thicknesses (see Supporting Information for the corresponding polarization and switching current loops).

are detected on the IR absorbance spectrum in Figure 3c, albeit with low intensities. These additional bands could be attributed to the strain induced during the releasing and transferring of the ZrO_2 film, as evident in the XRD results shown in Figure 3b. The transfer process primarily induced tensile strain in the film, influencing the unit cell angle and, to a very small extent, the lattice parameters of the *t*-ZrO_2 (Table 1). The strain effect on the IR absorbance of ZrO_2 has been previously discussed, and it was demonstrated that strain activates and amplifies new IR bands for the *t*-phase of ZrO_2.[46] It should here be underlined, that the IR absorbance can clearly be used to distinguish between different phases of ZrO_2, such as *r* , *o* , *t*, and *m* phases.[22,46] The presence of oxygen vacancies can also lead to the activation of additional IR bands. Evaluating the IR absorbance of the *t*-phase at an oxygen deficiency of 3.12%, we observed a response similar to that shown in Figure 3c, with a low intensity of the additional bands (Figure S12, Supporting Information). Thus, the lowest IR bands observed in Figure 3c can be influenced by both strain and oxygen vacancies. Based on the present results from XRD and IR absorbance, and in line with previous ones,[46] it is evident that ZrO_2 remains tetragonal under tensile strain, albeit with a small distortion observed in thinner films.

3.3. Ferroelectric Measurements

From our XRD and IR spectroscopy data (Figures 2 and 3), the investigated epitaxial ZrO_2 thin films in this study are shown to be in the t-phase. Electrically, these ZrO_2 films demonstrate ferroelectric properties up to a thickness of 31 nm. It is important to underline that, at variance with the study of Mimura et al.,[31] no field cycling is here needed to obtain a ferroelectric signature in our *t*-phase ZrO_2 epitaxial thin films. For instance, **Figure 4**a presents the P-E loops for the 15 nm thick ZrO_2 thin film in its pristine growth state, exhibiting a clear ferroelectric behavior with a polarization of 9 μC cm^{-2}. Notably, this polarization value is lower than the one reported for pure *r*-ZrO_2 films within the same thickness range (21 μC cm^{-2}).[23] This discrepancy can be attributed to the presence of compressive strain in the *r*-ZrO_2 phase,[23,30] whereas the films in our study are under small tensile strain. Nevertheless, Figure 4a unambiguously demonstrates the clear ferroelectric nature of the 15 nm thick ZrO_2 film. Similar P-E loops are obtained on all our films up to 31 nm thickness, and do not show any electric-field induced change upon repeated measurements. These observations hint that the observed ferroelectric behavior is not due to a phase change in the ZrO_2 thin films, for example from *t*-phase to *o*-phase as reported in Ref. [31].

The ferroelectric polarization of the ZrO_2 thin films was further investigated as a function of thickness (see Figures S8 and S9, Supporting Information, for the P-E loops). The remanent polarization (Pr) values are reported in Figure 4b, indicating that Pr gradually decreases with increasing film thickness. Specifically, the 7 nm thick ZrO_2 film exhibits a remanent polarization of 13 μC cm^{-2}, while the value reduces to 1 μC cm^{-2} for the 31 nm thickness. For the 42 nm thick ZrO_2 film, no ferroelectric behavior is observed, while a majority of *t*-phase is still detected by XRD. This suggests that the polarization decrease is a thickness effect on the *t*-phase itself, rather than being solely due to the formation of *m*-phase at the largest investigated thickness.

3.4. Discussion

In the case of pure ZrO_2, ferroelectricity has been reported in the *r*-phase[23,30] and in the *o*-phase, reports on the latter being the most numerous. Experimental studies on ZrO_2 polycrystalline thin films have shown polarizations in the 7–13 μC cm^{-2} range,[17,25,27,28] which is lower than the polarization theoretically predicted for the ZrO_2 *o*-phase, giving a high value above 50 μC cm^{-2}.[22,57] In epitaxial thin films of *o*-ZrO_2, a polarization of 27 μC cm^{-2} has been reported.[29] To our knowledge, the only report of ferroelectricity in *t*-phase ZrO_2 is from Mimura et al.[31]; however, the initial pristine film exhibited an antiferroelectric response, and after field cycling, the film became ferroelectric with a XRD signature from the *o*-phase.[31] In contrast, our films, as shown in Figure 4, exhibit wake-up free behavior, indicating that they are inherently ferroelectric. This wake-up free behavior has consistently been observed in epitaxial thin films, regardless of their phases.[16,23,29,30] However, none of the polar phases mentioned earlier were observed in our ZrO_2 films; instead, only a t-phase with tensile distortion was evidenced, suggesting that the induced ferroelectricity is primarily driven by substrate strain and thickness reduction effects. Indeed, from a consideration of

crystal symmetry, the *t*-phase itself is not intrinsically polar due to its centrosymmetric structure. Consequently, the observed ferroelectricity may not be intrinsic, and we now discuss some possible factors that could underlie its appearance.

Addressing the concept of strain-driven ferroelectricity, applying strain to the *t*-phase of ZrO_2 will lead to the disruption of its symmetry, potentially inducing polarization. For instance, a distorted *t*-phase characterized as the *Cm* monoclinic polar phase has theoretically demonstrated with a polarization close to that of the *r*-phase, alongside an IR response highly similar to the *t*-phase.[46] It is conceivable that this polarization might be further enhanced by strain, as observed for the *r*- and *o*-phases.[16,30,58] From our XRD data, as illustrated in Figure 1, a 7 nm thick ZrO_2 film does experience tensile strain, albeit at the modest level below 1%, and this could disrupt the symmetry of the *t*-phase and thus induce polarization.

Let us now address the possible impact of oxygen vacancies and oxygen migration in ZrO_2. Lenzi et al. investigated the influence of oxygen vacancies on the ferroelectric polarization of both the *r* and *t*-phases of ZrO_2, revealing that oxygen vacancies can indeed promote a polarization in the *t*-phase of ZrO_2.[24] However, at two distinct oxygen vacancy concentrations of 4.16% and 0.51%, the resulting polarization was found to remain lower than 1 μC cm^{-2}.[24] Thus, oxygen vacancies alone cannot account for the polarization levels measured in our ZrO_2 films (Figure 4). Another factor is electric-field induced oxygen migration. Experimental evidence in thin films of *r*-HZO and *o*-ZrO_2[59,60] has shown that oxygen migration can contribute to the measured ferroelectric hysteresis loops, particularly at reduced thicknesses (e.g., 5 nm). For a given applied voltage on a ZrO_2 capacitor, the electric field in the film should decrease with increasing thickness. This might provide an explanation for the observed decrease in polarization with increasing film thickness, as depicted in Figure 4b. However, a comprehensive investigation is required to fully assess the potential impact of oxygen migration and displacement in *t*-phase of ZrO_2 on the polarization hysteresis loops.

Furthermore, while our epitaxial thin films of ZrO_2 exhibit a ferroelectric behavior, antiferroelectricity has been reported in polycrystalline ZrO_2 thin films comprised of a majority of *t*-phase grains.[15,27,42] The occurrence of antiferroelectricity in polycrystalline films may potentially be related to their particular microstructure or grain boundaries, rather than being an intrinsic property of the ZrO_2 *t*-phase. More generally, further research is needed to uncover the complex interplay between microstructure, film growth, and the emergence of ferroelectricity or antiferroelectricity in ZrO_2 thin films.

4. Conclusion

We investigated the structure and ferroelectric behavior of epitaxial ZrO_2 thin films at different thicknesses grown on (110)-$SrTiO_3$ substrate. XRD results showed a *t*-phase of ZrO_2, with a small in-plane tensile strain detected in the thinner films. The *t*-phase of ZrO_2 was further confirmed by its characteristic IR absorbance spectrum. The films ranging from 7 to 31 nm thickness exhibited a clear ferroelectric behavior, right in their pristine state after growth, with a decreasing remanent polarization with increasing film thickness. Our experimental results demonstrate that ZrO_2 films with the XRD and IR spectroscopy signatures of the nonpolar *t*-phase exhibit ferroelectric behavior at reduced thickness. The origin of this ferroelectricity might thus be extrinsic, for example through the presence of oxygen vacancies or the influence of oxygen migration on ferroelectric measurements. These insights pave the way for exploring the origins of ferroelectricity in ZrO_2-based compounds and enhancing their performance for future applications.

Supporting Information

Supporting Information is available from the Wiley Online Library or from the author.

Acknowledgements

This work has received support from the Agence Nationale de la Recherche (ANR) under projects FOIST (N°ANR-18-CE24-0030) and FLEXO (N°ANR-21-CE09-0046), as well as from the French national network RENATECH for nanofabrication. Part of this work was granted access to the HPC resources of [CCRT/CINES/IDRIS] under the allocation 2021-2022 [AD010807031R1] made by GENCI (Grand Equipement National de Calcul Intensif). The authors also acknowledge the "Direction du Numérique" of the "Université de Pau et des Pays de l'Adour" and the mésocentre Aquitain (MCIA) for their computing facilities.

Conflict of Interest

The authors declare no conflict of interest.

Data Availability Statement

The data that support the findings of this study are available from the corresponding author upon reasonable request.

Keywords

epitaxy, ferroelectrics, infrared, tetragonal, zirconia, ZrO_2

Received: July 31, 2023
Revised: September 18, 2023
Published online:

[1] T. S. Böscke, J. Müller, D. Bräuhaus, U. Schröder, U. Böttger, *Appl. Phys. Lett.* **2011**, *99*, 102903.
[2] A. J. Bauer, M. Lemberger, T. Erlbacher, W. Weinreich, *Sci. Net.* **2008**, *573–574*, 165.
[3] K. J. Hubbard, D. G. Schlom, *J. Mater. Res.* **1996**, *11*, 2757.
[4] M. Copel, M. Gribelyuk, E. Gusev, *Appl. Phys. Lett.* **2000**, *76*, 436.
[5] J. Müller, T. S. Böscke, S. Müller, E. Yurchuk, P. Polakowski, J. Paul, D. Martin, T. Schenk, K. Khullar, A. Kersch, W. Weinreich, S. Riedel, K. Seidel, A. Kumar, T. M. Arruda, S. V. Kalinin, T. Schlösser, R. Boschke, R. van Bentum, U. Schröder, T. Mikolajick, in *2013 IEEE International Electron Devices Meeting*, IEEE, Piscataway, NJ **2013**, pp. 10.8.1–10.8.4.
[6] S. Roy, G. Niu, Q. Wang, Y. Wang, Y. Zhang, H. Wu, S. Zhai, P. Shi, S. Song, Z. Song, Z.-G. Ye, C. Wenger, T. Schroeder, Y.-H. Xie, X. Meng, W. Luo, W. Ren, *ACS Appl. Mater. Interfaces* **2020**, *12*, 10648.

[7] T. Ali, P. Polakowski, S. Riedel, T. Büttner, T. Kämpfe, M. Rudolph, B. Pätzold, K. Seidel, D. Löhr, R. Hoffmann, M. Czernohorsky, K. Kühnel, X. Thrun, N. Hanisch, P. Steinke, J. Calvo, J. Müller, *Appl. Phys. Lett.* **2018**, *112*, 222903.
[8] M. H. Park, H. J. Kim, Y. J. Kim, T. Moon, K. D. Kim, C. S. Hwang, *Adv. Energy Mater.* **2014**, *4*, 1400610.
[9] M. Hoffmann, M. Pešić, K. Chatterjee, A. I. Khan, S. Salahuddin, S. Slesazeck, U. Schroeder, T. Mikolajick, *Adv. Funct. Mater.* **2016**, *26*, 8643.
[10] S. Park, M. C. Chun, S. Park, G. yeon Park, M. Jung, Y. Noh, S.-E. Ahn, B. S. Kang, *Current Applied Physics* **2019**, *19*, 347.
[11] C.-H. Cheng, C.-C. Fan, C.-Y. Tu, H.-H. Hsu, C.-Y. Chang, *IEEE Trans. Electron Devices* **2019**, *66*, 825.
[12] Y. Wei, S. Matzen, T. Maroutian, G. Agnus, M. Salverda, P. Nukala, Q. Chen, J. Ye, P. Lecoeur, B. Noheda, *Phys. Rev. Appl.* **2019**, *12*, 031001.
[13] S. S. Cheema, N. Shanker, C.-H. Hsu, A. Datar, J. Bae, D. Kwon, S. Salahuddin, *Adv. Electron. Mater.* **2022**, *8*, 2100499.
[14] J. Müller, T. S. Böscke, U. Schröder, S. Mueller, D. Bräuhaus, U. Böttger, L. Frey, T. Mikolajick, *Nano Lett.* **2012**, *12*, 4318.
[15] M. H. Park, Y. H. Lee, H. J. Kim, Y. J. Kim, T. Moon, K. D. Kim, J. Müller, A. Kersch, U. Schroeder, T. Mikolajick, C. S. Hwang, *Adv. Mater.* **2015**, *27*, 1811.
[16] Y. Wei, P. Nukala, M. Salverda, S. Matzen, H. J. Zhao, J. Momand, A. S. Everhardt, G. Agnus, G. R. Blake, P. Lecoeur, B. J. Kooi, J. Íñiguez, B. Dkhil, B. Noheda, *Nat. Mater.* **2018**, *17*, 1095.
[17] S. Starschich, T. Schenk, U. Schroeder, U. Boettger, *Appl. Phys. Lett.* **2017**, *110*, 182905.
[18] S. J. Lee, M. J. Kim, T. Y. Lee, T. I. Lee, J. H. Bong, S. W. Shin, S. H. Kim, W. S. Hwang, B. J. Cho, *AIP Adv.* **2019**, *9*, 125020.
[19] R. Batra, T. D. Huan, G. A. J. Rossetti, R. Ramprasad, *Chem. Mater.* **2017**, *29*, 9102.
[20] S. Dutta, H. Aramberri, T. Schenk, J. Íñiguez, *Phys. Status Solidi Rapid Res. Lett.* **2020**, *14*, 2000047.
[21] M. H. Park, Y. H. Lee, H. J. Kim, T. Schenk, W. Lee, K. D. Kim, F. P. G. Fengler, T. Mikolajick, U. Schroeder, C. S. Hwang, *Nanoscale* **2017**, *9*, 9973.
[22] R. Materlik, C. Kunneth, A. Kersch, *J. Appl. Phys.* **2015**, *117*, 10897550.
[23] A. El Boutaybi, T. Maroutian, L. Largeau, S. Matzen, P. Lecoeur, *Phys. Rev. Mater.* **2022**, *6*, 074406.
[24] V. Lenzi, J. P. B. Silva, B. Šmíd, V. Matolín, C. M. Istrate, C. Ghica, J. L. MacManus-Driscoll, L. Marques, *Energy Environ. Mater.* **2022**, e12500.
[25] S. Shibayama, J. Nagano, M. Sakashita, O. Nakatsuka, *Jpn. J. Appl. Phys.* **2020**, *59*, SMMA04.
[26] K.-W. Huang, S.-H. Yi, Y.-S. Jiang, W.-C. Kao, Y.-T. Yin, D. Beck, V. Korolkov, R. Proksch, J. Shieh, M.-J. Chen, *Acta Mater.* **2021**, *205*, 116536.
[27] B. Xu, P. D. Lomenzo, A. Kersch, T. Mikolajick, U. Schroeder, *ACS Appl. Electron. Mater.* **2022**, *4*, 3648.
[28] A. P. S. Crema, M. C. Istrate, A. Silva, V. Lenzi, L. Domingues, M. O. Hill, V. S. Teodorescu, C. Ghica, M. J. M. Gomes, M. Pereira, L. Marques, J. L. MacManus-Driscoll, J. P. B. Silva, *Adv. Sci.* **2023**, *10*, 2207390.
[29] T. Song, H. Tan, N. Dix, R. Moalla, J. Lyu, G. Saint-Girons, R. Bachelet, F. Sánchez, I. Fina, *ACS Appl. Electron. Mater.* **2021**, *3*, 2106.
[30] J. P. B. Silva, R. F. Negrea, M. C. Istrate, S. Dutta, H. Aramberri, J. Iniguez, F. G. Figueiras, C. Ghica, K. C. Sekhar, A. L. Kholkin, *ACS Appl. Mater. Interfaces* **2021**, *13*, 51383.
[31] T. Mimura, T. Shimizu, O. Sakata, H. Funakubo, *Phys. Rev. Mater.* **2021**, *5*, 114407.
[32] R. C. Garvie, *J. Phys. Chem.* **1965**, *69*, 1238.
[33] R. C. Garvie, *J. Phys. Chem.* **1978**, *82*, 218.
[34] M. W. Pitcher, S. V. Ushakov, A. Navrotsky, B. F. Woodfield, G. Li, J. Boerio-Goates, B. M. Tissue, *J. Am. Ceram. Soc.* **2005**, *88*, 160.
[35] S. Riedel, P. Polakowski, J. Müller, *AIP Adv.* **2016**, *6*, 2158, 095123.
[36] X.-Q. Zheng, T. Tharpe, S. M. Enamul Hoque Yousuf, N. G. Rudawski, X.-L. Feng, Philip, R. Tabrizian, *ACS Appl. Mater. Interfaces* **2022**, *14*, 36807.
[37] O. Ohtaka, T. Yamanaka, S. Kume, N. Hara, H. Asano, F. Izumi, *Proc. Jpn. Acad. Ser. B* **1990**, *66*, 193.
[38] H.-J. Lee, M. Lee, K. Lee, J. Jo, H. Yang, Y. Kim, S. C. Chae, U. Waghmare, J. H. Lee, *Science* **2020**, *369*, 1343.
[39] A. Kersch, M. Falkowski, *Phys. Status Solidi Rapid Res. Lett.* **2021**, *15*, 2100074.
[40] L. Azevedo Antunes, R. Ganser, C. Kuenneth, A. Kersch, *Phys. Status Solidi Rapid Res. Lett.* **2022**, *16*, 2100636.
[41] S. E. Reyes-Lillo, K. F. Garrity, K. M. Rabe, *Phys. Rev. B* **2014**, *90*, 140103.
[42] Z. Wang, A. A. Gaskell, M. Dopita, D. Kriegner, N. Tasneem, J. Mack, N. Mukherjee, Z. Karim, A. I. Khan, *Appl. Phys. Lett.* **2018**, *112*, 222902.
[43] H. Dahlberg, A. E. O. Persson, R. Athle, L.-E. Wernersson, *ACS Appl. Electron. Mater.* **2022**, *4*, 6357.
[44] P. D. Lomenzo, L. Collins, R. Ganser, B. Xu, R. Guido, A. Gruverman, A. Kersch, T. Mikolajick, U. Schroeder, *Adv. Funct. Mater.* 2303636.
[45] R. Dovesi, A. Erba, R. Orlando, C. M. Zicovich-Wilson, B. Civalleri, L. Maschio, M. Rérat, S. Casassa, J. Baima, S. Salustro, B. Kirtman, *WIREs Comput. Mol. Sci.* **2018**, *8*, e1360.
[46] A. El Boutaybi, R. Cervasio, A. Degezelle, T. Maroutian, J.-B. Brubach, V. Demange, L. Largeau, M. Verseils, S. Matzen, G. Agnus, L. Vivien, P. Karamanis, M. Rérat, P. Roy, P. Lecoeur, *J. Mater. Chem. C* **2023**.
[47] S. Maletic, D. Maletic, I. Petronijevic, J. Dojcilovic, D. M. Popovic, *Chin. Phys. B* **2013**, *23*, 026102.
[48] P. Roy, M. Rouzières, Z. Qi, O. Chubar, *Infrared Phys. Technol.* **2006**, *49*, 139.
[49] P. Jiao, J. Li, Z. Xi, X. Zhang, J. Wang, Y. Yang, Y. Deng, D. Wu, *Appl. Phys. Lett.* **2021**, *119*, 252901.
[50] Y. Yun, P. Buragohain, M. Li, Z. Ahmadi, Y. Zhang, X. Li, H. Wang, J. Li, P. Lu, L. Tao, H. Wang, J. E. Shield, E. Y. Tsymbal, A. Gruverman, X. Xu, *Nat. Mater.* **2022**, *21*, 903.
[51] T. Song, H. Tan, S. Estandía, J. Gàzquez, M. Gich, N. Dix, I. Fina, F. Sánchez, *Nanoscale* **2022**, *14*, 2337.
[52] K. Liu, F. Jin, X. Zhang, K. Liu, Z. Zhang, E. Hua, J. Zhang, H. Ye, G. Gao, C. Ma, L. Wang, W. Wu, *Adv. Funct. Mater.* **2023**, *33*, 2209925.
[53] S. Estandía, N. Dix, M. F. Chisholm, I. Fina, F. Sánchez, *Cryst. Growth Des.* **2020**, *20*, 3801.
[54] E. H. Kisi, C. J. Howard, *Key Eng. Mater.* **1998**, *154*, 1.
[55] E. Bonera, G. Scarel, M. Fanciulli, *J. Non-Cryst. Solids* **2003**, *322*, 105.
[56] A. Kersch, R. Ganser, M. Trien, *Front. Nanotechnol.* **2022**, *4*, 2673.
[57] A. El Boutaybi, P. Karamanis, T. Maroutian, S. Matzen, L. Vivien, P. Lecoeur, M. Rérat, *Phys. Rev. B* **2023**, *107*, 045140.
[58] S. Estandía, N. Dix, J. Gazquez, I. Fina, J. Lyu, M. F. Chisholm, J. Fontcuberta, F. Sánchez, *ACS Appl. Electron. Mater.* **2019**, *1*, 1449.
[59] P. Nukala, M. Ahmadi, Y. Wei, S. de Graaf, E. Stylianidis, T. Chakrabortty, S. Matzen, H. W. Zandbergen, A. Björling, D. Mannix, D. Carbone, B. Kooi, B. Noheda, *Science* **2021**, *372*, 630.
[60] X. Li, H. Zhong, T. Lin, F. Meng, A. Gao, Z. Liu, D. Su, K. Jin, C. Ge, Q. Zhang, L. Gu, *Adv. Mater.* **2023**, *35*, 2370196.